InterPore JOURNAL

Original Research

EVAPORATION IN THE PRESENCE OF PARTICLES IN A MODEL POROUS MEDIUM: IMPACT OF CORNER LIQUID FILMS

Elisa Ghiringhelli[1], Manuel Marcoux[1], Sandrine Geoffroy[2], Marc Prat[1]

[1]*Institut de Mécanique des Fluides de Toulouse (IMFT), Université de Toulouse, CNRS – Toulouse, France;* [2]*LMDC (Laboratoire Matériaux et Durabilité des Constructions), Université de Toulouse, INSAT, UPS, France*

Correspondence to:
Marc Prat: mprat@imft.fr

How to Cite:
Ghiringhelli, E., Marcoux, M., Geoffroy, S., & Prat, M. (2024). Evaporation in the presence of particles in a model porous medium: impact of corner liquid films. *InterPore Journal*, *1*(1), ipj260424–4. https://doi.org/10.69631/ipj.v1i1nr12

RECEIVED: 11 Oct. 2023
ACCEPTED: 25 Mar. 2024
PUBLISHED: 26 Apr. 2024

@2024 The Authors

ABSTRACT

Visualization experiments with a microfluidic channel network (micromodel) were performed to study evaporation in the presence of colloidal particles. Comparisons were then performed, changing the wetting properties of the micromodel thanks to a plasma treatment. It was found that the most hydrophilic micromodel led to a faster drying and a different final distribution of the deposited particles within the channel network compared to the less hydrophilic micromodel. This is explained by the impact of capillary liquid films forming in corners of the channels. The observations suggest that the liquid corner films form a better-connected sub-network in the case of the more hydrophilic network providing a pathway for the transport of particles. As indicated by the longer drying, the corner film subnetwork is less well-connected in the less hydrophilic network, which eventually leads to a quite different final particle deposit pattern.

KEYWORDS

Colloidal suspension, Evaporation, Corner liquid films, Micromodal, Wettability

This is an open access article published by InterPore under the terms of the Creative Commons Attribution-NonCommercial-NoDerivatives 4.0 International License (CC BY-NC-ND 4.0) (https://creativecommons.org/licenses/by-nc-nd/4.0/).

1. INTRODUCTION

Drying of porous media has been the subject of several studies since the early works of Lewis (28) or Sherwood (46). As reviewed in one study (52), the drying of a pure liquid in a porous medium is still a very active research topic, not only because drying is a frequently encountered step in many industrial fabrication processes, but also because predicting a full drying cycle is still a challenge from a scientific and modelling perspective. However, in many cases, the situations of interest are not limited to the consideration of a pure volatile liquid, and much more complex cases have been studied. These include situations where a multicomponent liquid (9), one or more dissolved salts (12, 27, 32, 38, 41, 47), or other dissolved species (42), polymers (13) or particles (22, 23, 39, 40) are present in the pore space. In a drying problem with a pure liquid, the main objectives are to characterize the liquid distribution in the porous medium during drying and the evaporation kinetics, i.e. the variation of the evaporation rate as a function of the liquid content in the porous medium (52), considering situations where there is no structural

impact on the porous matrix integrity during drying (8, 18). When a species is present in the liquid, an additional major objective is the characterization of the distribution of the dissolved species during drying (19, 43). When the species can precipitate (e.g. a dissolved salt) (10), or form agglomerates or deposits (e.g. particles), the localization of the precipitated species (10, 42) or the particle clusters (39, 40) in the pore space becomes of great interest, especially in relation to applications (20, 42) where control of the localization of the precipitated species within the porous medium is a major concern.

In this context, the present study aims at contributing a better understanding of the drying process in the presence of colloidal particles. The focus being on the potential impact of corner liquid films on the transport of colloidal particles within the porous medium during drying and the impact of this transport on the final localization of the particles in the pore space at the end of drying. These films, also referred to as capillary thick films (54), form in crevices or corners in the pore space. As reported in one study (4), drying is much faster in a single capillary square tube compared to drying in a circular tube due to the presence of capillary liquid films along the inner corners of the square tube. Such an enhanced evaporation effect was also reported in a packing of grains confined between two plates (55), or in micromodel experiments (26). Therefore, these films can presumably form a pathway for the particle transport. However, as pointed out in another study (51), these films do not always form a well-connected subnetwork in the pore space, and can instead take the form of isolated capillary rings (24, 44, 48) around solid blocks in micromodels (48), or in the contact areas between grains (24, 44).

To obtain insight into the possible impact of corner films on the transport of particles during drying, evaporation experiments in the presence of a colloidal suspension are performed with a model porous medium consisting of a square network of interconnected channels. As discussed in (52), micromodels are a classical tool to study evaporation processes in porous media, (5, 6, 14, 15, 25, 26, 29, 32, 42, 44, 48, 49, 51, 53) with the advantage of allowing direct visualization of the evolution of the liquid and gas phases during drying. Corner films are often discussed in these studies with micromodels. For instance, the presence of the corner films is inferred in two studies (26, 36) from comparisons between experiments and pore-network simulations, but without explicit visualizations of the corner films in the experiments. Capillary rings and capillary bridges are visualized in (14) but the emphasis in this paper is not on the film effect, which is limited in the considered experiments. Chains of capillary bridges between pillars have also been visualized and studied (5, 6). It is shown that drying can be much faster when the pillars are distributed to favor the formation of long capillary bridge chains. Liquid bridges and corner liquid rings are visualized in one study (48) over a few channels, and a pore network model considering the liquid rings is developed. Regions of the micromodel where corner films are present are identified in another study (43) at the scale of the micromodel, however individual corner films are not visualized, and the emphasis is on the salt deposition. A distinction has also been made between continuous and discontinuous corner films (52). The former are corner films connected to bulk liquid whereas the latter are not. The two types of corner films are inferred from visualizations in a small micromodel. A detailed analysis of the impact of both types of corner films is proposed and a pore network model considering the corner films is developed. The interplay between salt precipitation and corner films was studied by Wu and Chen (53). It is shown that the impact of corner films on the salt deposition is significant. However, the corner films are not directly visualized in the considered micromodels. The corner films are the main focus in another paper by Geistlinger et al. (15). The corner flow region in the micromodel is visualized, and corner flow paths are identified. It has also been shown that the corner films are sensitive to the wetting conditions (15, 36). The lower the contact angle, the thicker the corner films are for a given geometry, a principle valid for sufficiently low contact angles. Conversely, if the contact angle is too high (above 45° in a right-angle corner of uniform wettability), the corner films cannot develop (36). For this reason, comparisons are performed changing the wetting conditions in the micromodel thanks to a plasma treatment.

2. MATERIALS AND METHODS

2.1. Micromodel

As depicted in **Figure 1**, the model porous medium, also referred to as the micromodel, consists of a square network of interconnected channels of rectangular cross section. As sketched in **Figure 1b**, the depth of the channel is uniform and equal to 1 mm whereas the channel width varies between 80 µm and 910 µm according to a uniform probability density function. The distance between two nodes (channel intersections) in the network is 3 mm. The channel length varies between 2.6 and 3 mm. The total dimension of the micromodel is 1.8 cm × 1.9 cm. As illustrated in **Figure 1b**, the micromodel is composed of a SUEX™ dry film photoresists[a] layer in which the channel network is located. The micromodel is closed with a polydimethylsiloxane[b] (PDMS) layer, covered in turn by a thin glass slide. Therefore, the channels have three sides made of SUEX, while the top wall is PDMS. The micromodel is held horizontally in all the experiments discussed in the present article. Thus, gravity effects on the liquid-gas pattern forming in the micromodel are negligible.

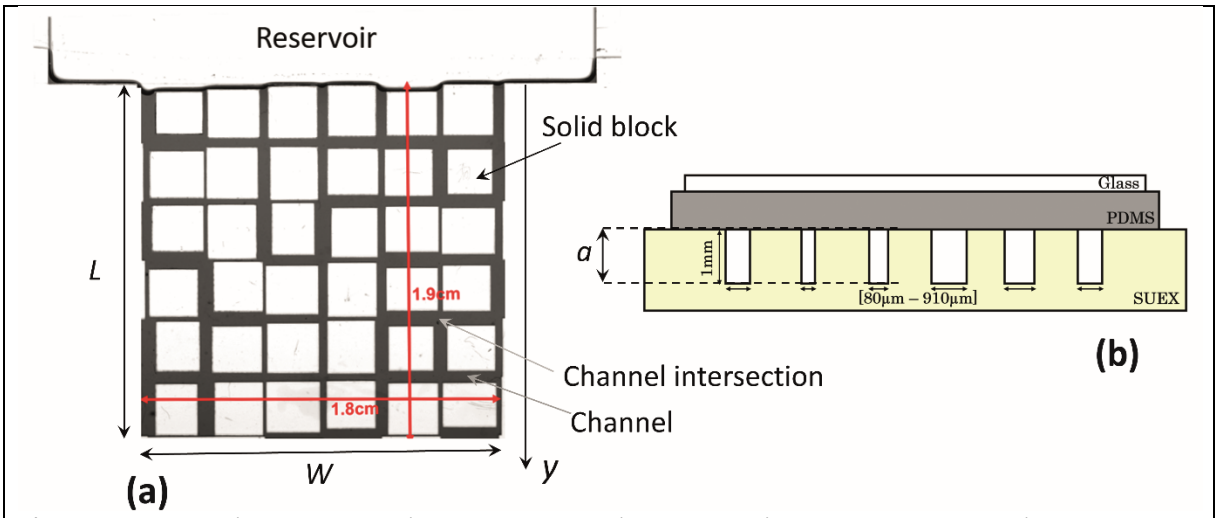

Figure 1: (a) Top view of composite SUEX-PDMS micromodel with square network of interconnected channels of the rectangular cross section. The image is with liquid (in black) in the channels. **(b)** Sketch of a cross section of the micromodel with the various layers; the PDMS is colored grey for illustration, but in reality it is transparent.

2.2. Experimental protocol

Evaporation experiments were performed by filling the micromodel with either pure water or a colloidal dispersion of water with particles. The particles were carboxylate-modified fluorescent microspheres of 1 µm in diameter[c] available in a solution of distilled water containing particles at a concentration of 2% (g/mL). The particle concentration (in g/mL) in the considered experiments is 0.5 × 10−4 g/mL. This concentration was obtained by mixing a given volume of the 2% (g/mL) solution with a selected volume of water so as to obtain the desired concentration. The procedure for saturating the micromodel with liquid is as follows. The micromodel was cleaned with ethanol, dried with compressed air, and closed with the layer of PDMS. The latter was placed on the SUEX layer, paying attention to avoid any residual bubble between the two layers. The PDMS material was chosen for its properties such as the optical transparency and flexibility. As it is known that water can pervaporate through PDMS (31), the PDMS was covered with a thin glass slide that stuck to it without requiring any surface treatment. Once the setup is ready, the reservoir in front of the channels (**Fig. 1a**) was filled with pure water or the colloidal

[a] SUEX™ dry film photoresists: produced by DJ MIcrolaminates (https://djmicrolaminates.com/); purchased from: MicroResist Technologies (https://www.microresist.de/)
[b] PDMS (Sylgard 184, ref : DC184-1.1): Neyco (https://www.neyco.fr)
[c] Molecular ProbesTM Fluo 3 (maximum absorption 580 nm, approx. emission 605 nm, density of 1.05 g/mL): produced by Life Technologies Corporation, but bought from ThermoFisher Scientific

dispersion, thus closing all outlets. The micromodel was then placed in a vacuum jar in which the pressure was reduced to 100 mbar for a few minutes. Next, as the pressure slowly rises back to the atmospheric pressure, the liquid fills in the channels. This process, taking the micromodel under vacuum conditions and slowly back to atmospheric pressure, was repeated two or three times until the micromodel was completely saturated by liquid.

2.3. Drying setup

Drying experiments require controlling the temperature and relative humidity of the atmosphere in contact with the micromodel. To this end, experiments are performed in a room where the temperature is kept constant thanks to an automatized air conditioner set to 22°C. However, the air conditioner control system leads to some fluctuations around the selected temperature value. To damp out these fluctuations the micromodel was set in a box made of Plexiglas panels. One of these panels can be opened to set the micromodel in the box. The other panels are hermetically sealed together. In the box, the micromodel was set on a 10^{-4} g precision balance[d] to measure the evolution of the liquid mass. Mass data was recorded every 10 seconds. In addition, a thin support was set on the balance to hold the micromodel, which was set horizontally on the support. In between, a back light triggered by the camera (see below) was set for better visualization. The back light was set in such a way that it did not touch the balance pan so as not to impact the weight measurements. More details and images of the set-up can be found in a previous paper from Ghiringhelli (16).

The relative humidity (RH) was kept at 7-8 % in the box thanks to a saturated Lithium Bromide solution filling two open channels along the sides of the balance. As soon as the box is closed a small fan is turned on for about 10 minutes to speed up the process of decreasing the humidity to approximately 10%, after which point the fan is turned off. Both the temperature and the relative humidity were recorded every five minutes thanks to a sensor placed inside the box near the top panel.

The evolution of the liquid distribution in the micromodel during drying was recorded by a Nikon camera D700 equipped with a macro lens. The camera was controlled by a computer via the Camera Control Pro 2 software, and the images were acquired at a time interval of two minutes. To increase the contrast between air and water, namely, to obtain better visualization of the fluid distribution in the micromodel, dye was added to pure water. More precisely, 0.0065 g of fluorescein is added to 45 g of water. This corresponds to a concentration of 0.01% which is sufficiently low for the corresponding nanoparticles, documented to be oblate ellipsoid with approximate volume of 0.4 nm^3 (37), and to not change the dynamics of the drying process. It can be noted that the 3D structure of the corner films was not considered when the overall saturation was determined from a 2D image. This introduces a slight overestimate of the saturation.

2.4. Plasma treatment

A plasma treatment was performed to improve the adhesion of the PDMS layer onto the SUEX layer. The SUEX and PDMS layers composing the micromodel were set in the plasma cleaner chamber[e] for seven minutes at high power using a temperature close to the ambient temperature, after which the treated surfaces were assembled together.

A consequence of the plasma treatment is the modification of the wettability properties of the materials. As reported in (17), the contact angle of water on untreated SUEX is approximately 75°. As indicated in **Figure 2**, the plasma treated SUEX becomes much more hydrophilic, with an equilibrium contact angle of 27.4° on average. The contact angle was also measured during the evaporation of a droplet right after the plasma treatment. The contact angle was found to be equal to 34.6° at the very beginning of the evaporation, after which it dropped to 4.6° in about 20 minutes, as shown in **Figure 2**,. Performing a similar measurement after leaving the SUEX at ambient temperature and atmospheric pressure for 20

[d] Quintix Balance (Quintix224-1S): Sartorius Lab Instruments GmbH & Co. KG, Göttingen, Germany
[e] Expanded plasma cleaner PDC-002 (230V): Harrick Plasma, Ithaca, NY, USA

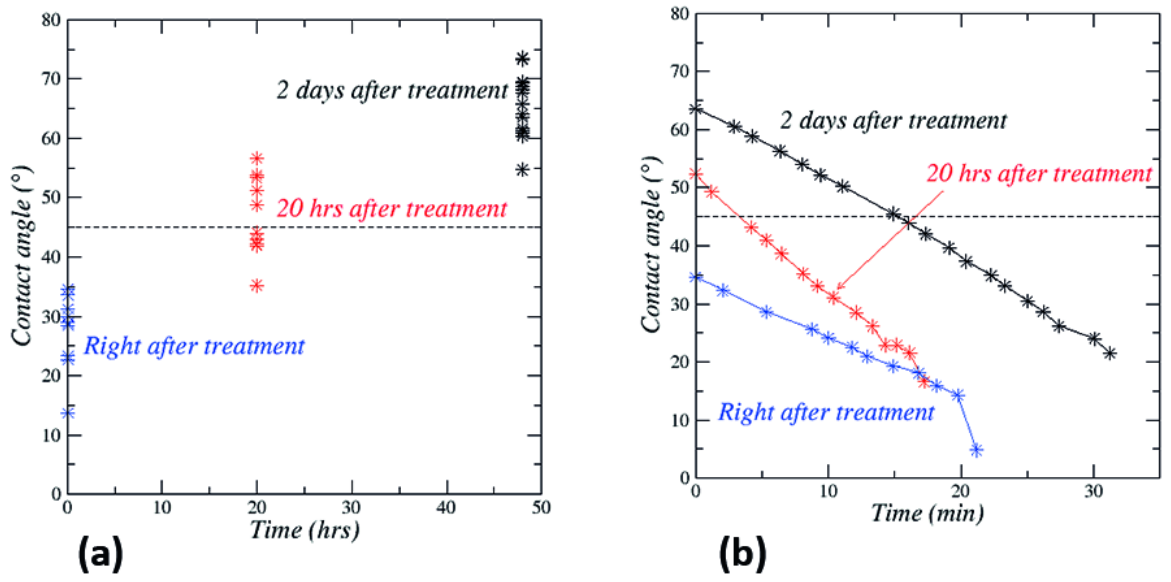

Figure 2: (a) Equilibrium contact angle on SUEX right after the plasma treatment, after 20 hours, and after 48 hours. **(b)** Evolution of the contact angle of an evaporating droplet of water set on a layer of SUEX treated with plasma. The horizontal dashed line corresponds to the contact angle value (45°) above which corner films cannot develop in a right angle.

hours led to the following results: the contact angle was 47° at the beginning of the experiment and decreased down to less than 20° in 20 minutes (**Fig. 2**).

After 48 hours of exposition to the ambient conditions, the equilibrium contact angle was found to be 65°, approaching the value obtained without any treatment (17). As reported in one study (17), fresh PDMS is hydrophobic (θ ≈ 104° for pure water, where θ is the contact angle) but the contact angle tends to decrease over time and can become less than 90° in evaporative droplet experiments (17). As reported in another study (1), the plasma treatment on PDMS considerably reduces the contact angle which can become lower than 45°. As for SUEX, the contact angle then increases, and after a few hours, the impact of the plasma treatment on the contact angle becomes negligible (1). As Prat discussed in one study (36), the value of 45° for the contact angle is a limit for the corner liquid films to form in right angle corners. Corner films cannot develop when the contact angle is greater than 45°. Based on the data reported in **Figure 2a** for SUEX and in (1) for PDMS, it is therefore tempting to consider that corner films can only form in experiments performed right after the plasma treatment. However, based on the data reported in **Figure 2b** as well as experiments performed in a single SUEX-PDMS channel (17), it is indicated that corner films can be present in experiments performed long after the plasma treatment occurred as the receding contact angle can become less than 45° on SUEX after a sufficient time period has passed (**Fig. 2b**). The results presented in (17) indicate that corner liquid films can indeed form in the SUEX corners, but not in the SUEX-PDMS corners, when the experiment is performed after a sufficient time period has passed since the plasma treatment. In other words, corner films can be expected both in experiments performed right after the plasma treatment and long after the plasma treatment, however, the thickness of the corner films is expected to be significantly greater in the experiments performed right after the plasma treatment (the lower the contact angle becomes below 45°, the thicker the corner film becomes) (36). However, it is possible that corner films form in the four corners of the channel in the experiment performed right after the plasma treatment, whereas corner films are expected only in the SUEX corners in the case of the experiment performed long after the plasma treatment. Finally, it can be noted that the film continuity over the micromodel cannot be inferred from the experiments in a single channel (17) because the corner continuity is not maintained in the channel intersections in the micromodel.

2.5. Imaging the deposit: particle deposit image processing

After the water has completely evaporated in the micromodel, and the particles have deposited, the micromodel is opened and set under a microscope[f] equipped with a confocal green light, a 5x/0.16Phl lens, and a camera[g] in order to obtain images of the final particle deposit in the micromodel. To this end, the micromodel is scanned from the upper left corner row by row. For each row, the same number of images is selected. Then, the Grid/Collection stitching plugin of Fiji[h] is used to recompose the image of the deposit at the bottom of the whole channel network. Since the images at the microscope are taken manually, different tile overlaps, usually around 50%, must be tested to obtain the whole image. Additional information on this procedure is presented in **Appendix A** (available online), see also (16).

3. RESULTS

3.1. Overall saturation variation

The variations of the overall liquid saturation as a function of time for the three considered experiments are compared in **Figure 3**. As can be seen, the saturation variation is quite similar between the pure water case and the case with particles for the experiments performed one month after the plasma treatment. Thus, the impact of particles on the drying kinetics is negligible for the considered concentration in particles. Interestingly, the drying is considerably faster in the case of the experiments performed right after the plasma treatment. This is consistent with the expected effect of corner films based on the consideration that lower contact angles should lead to thicker films (**Fig. 4**) and a better-connected corner film sub-network with a greater hydraulic conductivity. This point is further investigated in the next section.

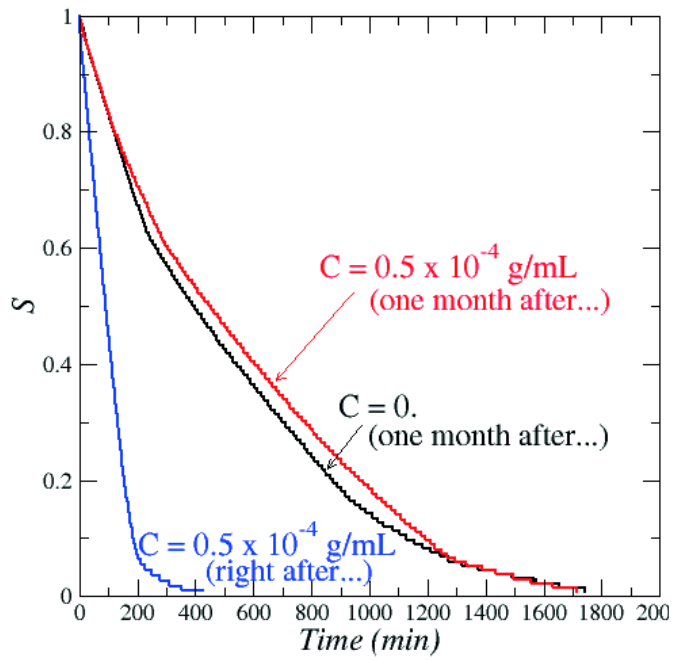

Figure 3: Variations of the overall liquid saturation as a function of time for the experiments being performed one month after the plasma treatment versus right after the plasma treatment.

3.2. Estimate of corner film spatial extent in the micromodel

The above considerations on the corner films can be further supported using the corner film model presented in previous works and references therein (see 36, and references therein). For the values of contact angle reported in **Figure 2,** and the measured evaporation rates, the objective is to explore quantitatively whether the corner film flow can develop over the full micromodel extent, or at least over a significant region of the micromodel. This model is analogous to a corner film model in a bundle of straight channels of polygonal cross sections (rectangular here). This means that this model does not consider the channel intersections, which are a place where the film continuity is less obvious than in the individual channels. Nevertheless, it provides an indication and, at least, an upper bound in terms of film thickness and film continuity over the micromodel. The model is summarized in **Appendix B** (available

[f] Zeiss Axio Scope.A1: ZEISS Microscopy
[g] LaVision Image sCMOS: LaVision
[h] Available at: https://imagej.net/software/fiji/downloads

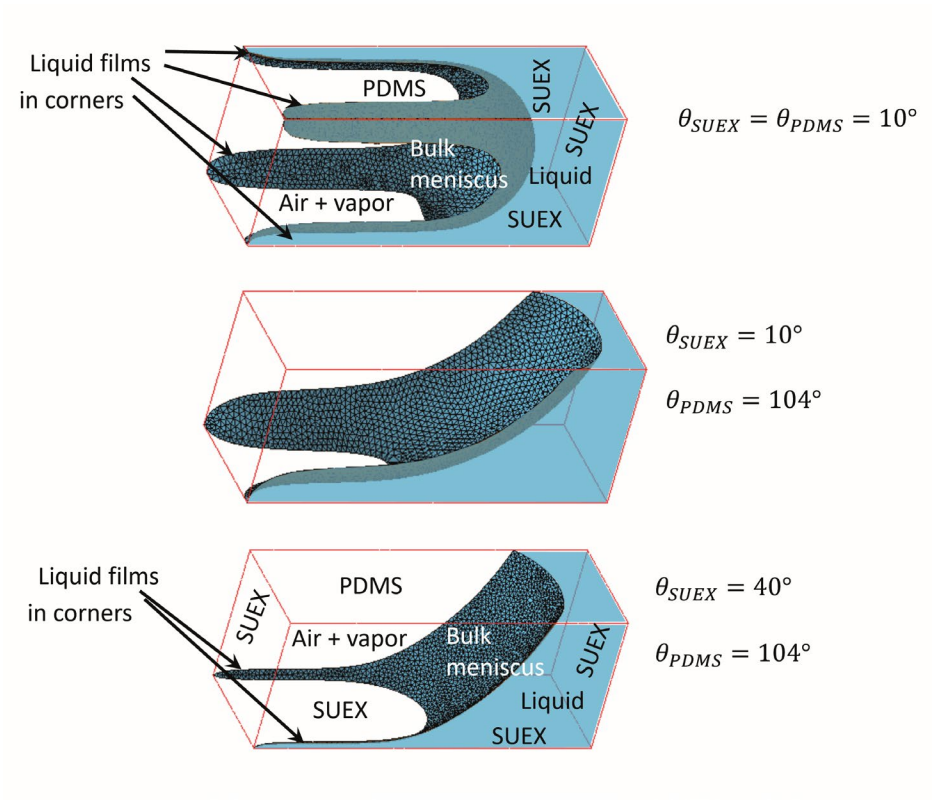

Figure 4: Illustration of impact of contact angle on corner liquid films in a channel with right angle corners. Quasi-static liquid-gas interface computed using the open-source software "Surface Evolver" (2); Films are thicker for a lower contact angle. Films can form in the four corners if the contact angle is lower than 45° on both PDMS and SUEX.

(Software available at: https://kenbrakke.com/evolver/evolver.html)

online). The maximum spatial extent $L_{film-max}$ of the corner film can be estimated from this model as a function of the evaporation flux, contact angle and the channel geometrical properties (see **Equation 10** in **Appendix B**, available online). The results are presented in **Figure 5**, where L is the micromodel spatial extent (L =1.9 cm, see **Fig. 1a**)

As can be seen from **Figure 5a**, the maximum corner film length depends highly on the contact angle and the channel width. For the contact angle nominal value of 30° (**Fig. 2a**), the corner film can develop over the entire micromodel length for most of the channel width. The maximum extent of the corner film is less than the micromodel length only for the channels with a width of less than 140 µm. For a contact angle of 10° or less (**Fig. 2b**), the maximum corner film extent is greater than the micromodel length for all channel widths. For a greater contact angle (40° in **Fig. 5a**), the film corner can develop over the full micromodel length only for the larger channel widths in the range of 600 µm - 910 µm.

The film thickness (see inset in **Fig. 5b**) can be expressed as shown in **Equation 1**, where $R(y)$ is the curvature radius of the corner film liquid-gas interface and y is the distance from the reservoir-micromodel interface, **Fig. 1a**).

$$w_{film}(z) = (\cos\theta - \sin\theta)R(y) \tag{1}$$

Considering again the nominal contact angle value of 30°, the variation of the film thickness (in µm) as a function of y is shown in **Figure 5b** for a few channel widths. As can be seen, the maximum corner film thickness varies between about 17 µm for the narrowest channel considered in **Figure 5b** to 130 µm for the largest channel. Roughly, the maximum film thickness (for one corner film) scales as $w/6$, where w

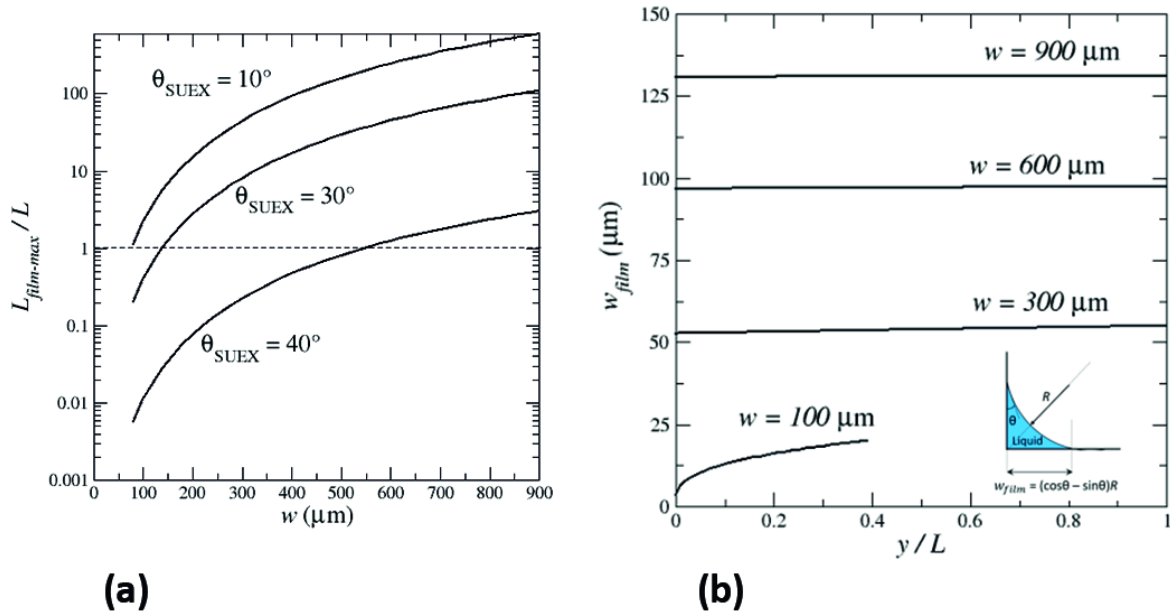

Figure 5: a) Maximum length of corner films resulting from the competition between viscosity and capillarity effects as a function of channel width for the three contact angle values. **(b)** The variation of corner film thickness over the micromodel length for the various channel widths when θ = 30°. When w = 100 μm, the film thickness distribution is shown when the corner films are about to recede into the channel.

is the channel width. As illustrated in this figure, the film thickness varies little along the channel for $w \geq 300\mu m$. As illustrated in **Figure 5**, the corner films cannot develop of the full length of the micromodel when w < 140 μm. Nevertheless, the narrower channels in the range [80 μm – 140 μm] can sustain the flow over a significant fraction of the micromodel length (**Fig. 5**). The mean channel width in the micromodel is expected to be close to 495 μm (the actual mean value can differ slightly due to the small number of channels in the micromodel). Based on the results illustrated in **Figure 5,** and the fact that the contact angle can be expected to be lower than 30° (**Fig. 2b**), one can conclude that the present results are fully consistent with a corner film network stretching over the full micromodel in the case of the micromodel right after the plasma treatment. The sensitivity of the results to the contact angle illustrated in **Figure 5** is consistent with the consideration that the corner films are significantly thinner, and possibly much less well connected in the case of the micromodel two months after the plasma treatment.

3.3. Drying pattern

Liquid and gas distributions (patterns) during drying between the case with particles one month after the plasma treatment and the case with particles right after the plasma treatment are compared in **Figure 6**. In **Figure 6**, S is the saturation, i.e. the volume fraction of the pore space occupied by liquid.

In the absence of gravity forces, two forces are expected to have an impact on the pattern: the capillary forces and the viscous forces (35).

The competition between both forces is characterized by the capillary number, which is defined as $Ca = \frac{\mu j}{\rho \cdot \gamma \cos\theta}$ (35), where μ is the liquid viscosity, γ is the surface tension, ρ is the liquid density, and j is the evaporation flux. For the values of evaporation flux than can be deduced from the data shown in **Figure 3**, $Ca \sim 10-9$ in the case of the experiment performed one month after the plasma treatment and $Ca \sim 10-8$ for the experiment performed right after treatment with plasma. For such a low capillary number value, the capillary forces are dominant. Under these circumstances, an invasion percolation (IP)

pattern (30, 50), is expected in a hydrophilic network (3, 7). Then, as previously described (35), drying proceeds according to a capillarity-controlled mechanism where the interfacial channels (the channels with a meniscus) of largest size are preferentially invaded. This is visible in **Figure 6** (look at the invasions in the first row of channels). Although the pattern is still of IP type in the case of the experiment performed directly after plasma treatment, and globally quite similar to the patterns for the experiment performed one month following plasma treatment, some differences are visible. For instance, with a saturation value of 0.5, in experiments performed one month after the plasma treatment, some channels were invaded with particles in the first row, whereas in the experiments performed directly following plasma treatment, these channels are still liquid filled. A more striking difference lies in the markedly improved solid block edge sharpness in the images corresponding to the experiment performed right after the plasma treatment. This is more clearly illustrated in **Figure 7** which shows a magnified view of the patterns for the two experiments with particles for S = 0.4. The solid block edges in the red dashed box in **Figure 7** are evidently more sharply defined in the experiment performed right after the plasma treatment. This is interpreted as an effect of the corner films. According to the contact angle discussion from the Section 2.4, corner films are expected in the experiment performed right after the plasma treatment. The prolonged presence of thicker films could account for the enhanced sharpness, potentially attributed to the existence of corner films in the upper corners of the channels.

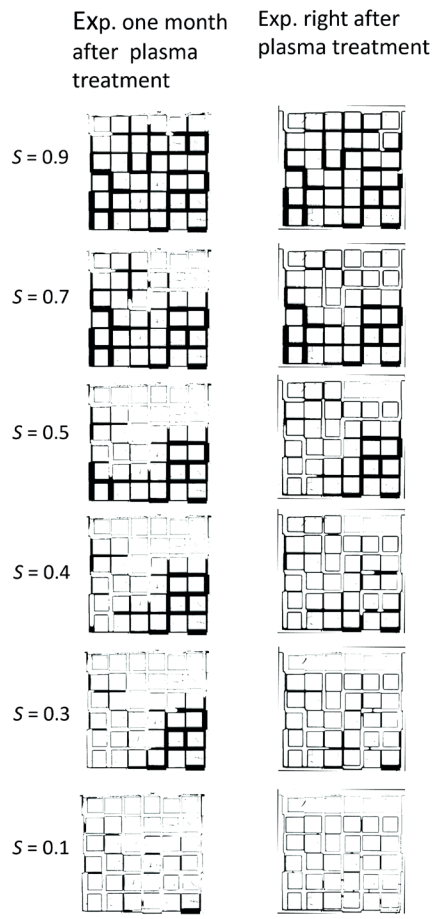

Figure 6: Comparison of drying patterns for liquid saturation S = 0.9, 0.7 and 0.5 (from left to right) for the experiments performed one month after the plasma treatment and the experiment performed right after the plasma treatment. The liquid phase is shown as black and the gas phase as white; vapor escapes through top edge of micromodel. The cell is held horizontally.

In complement, it can be seen in **Appendix C** (available online) that the patterns for the case of the experiments performed one month after the plasma treatment for pure water and with particles respectively are quite similar. Thus, the presence of the particles does not noticeably affect the pattern for the considered particle concentration, which is consistent with the weak impact of the particle presence on the drying curves in **Figure 3** (comparison of black and red curves).

3.4. Drying kinetics

Drying is often discussed in terms of drying kinetics (21), which is the plot of the evaporation rate as a function of the overall saturation. The idea with the drying kinetics is to combine the information on the patterns (**Fig. 6**) and the associated saturation with the information on the evaporation rate (which can be deduced from the results shown in **Fig. 3**). The drying kinetics for each experiment with particles is shown in **Figure 8**. The latter is obtained from polynomial fittings of the overall saturation variations, as shown in **Figure 3** (blue or red curves). Then $\frac{dS}{dt}$, as shown in **Figure 8**, is obtained by deriving the polynomial fitting corresponding to each experiment. The evaporation rate J is proportional to $\frac{dS}{dt}\left(J = \varepsilon\rho_\ell AH\frac{dS}{st}\right)$, where ε is the micromodel porosity (ε = 0.5), ρ_ℓ is the suspension density, H is the

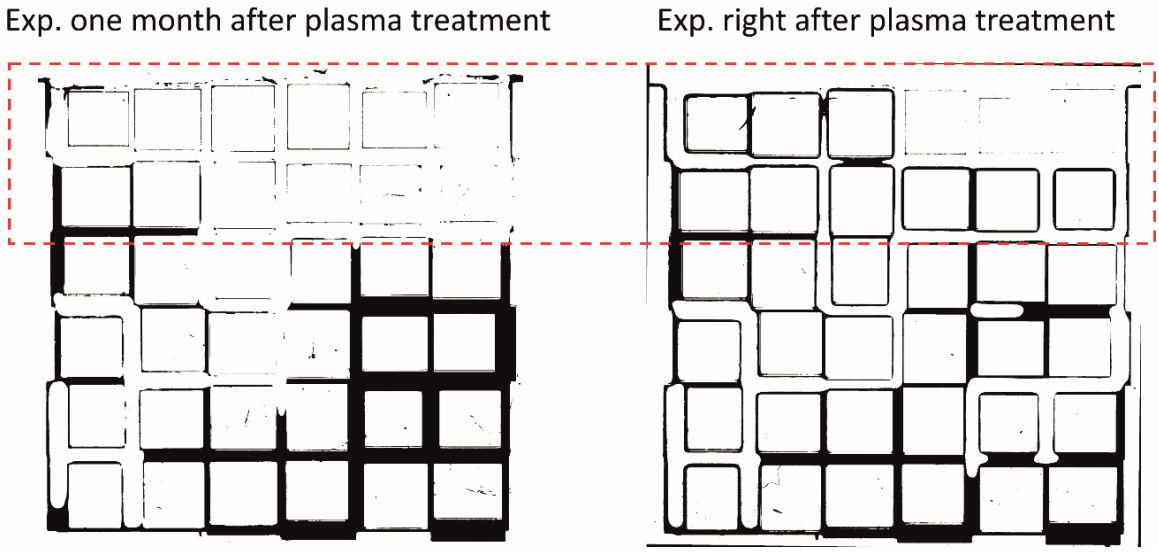

Figure 7: Drying pattern for S=0.4 for the two experiments with particles. The solid block edges in the red dashed box are much cleaner and more marked in the experiment performed right after the plasma treatment. This is a signature of the corner film presence.

micromodel height (1.9 cm, **Fig. 1a**) and A is the cross-section surface area of the micromodel). The variation of J can thus be discussed from the plots of $\frac{dS}{dt}$.

The evaporation rate, i.e. $\frac{dS}{dt}$ in **Figure 8**, is significantly greater in the experiment performed right after the plasma treatment. This is another illustration that drying is much faster in the experiment directly following plasma treatment.

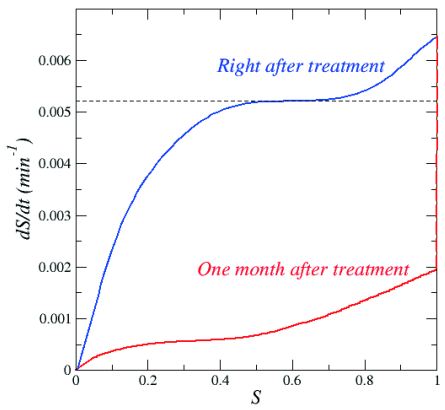

Figure 8: Drying kinetics: variation of drying rate as a function of overall saturation for the two experiments with particles.

This is consistent with the patterns shown in **Figure 6** and **Figure 7**. For instance, once can compare the patterns between the two experiments with particles for S = 0.4 in **Figure 7**. Based on the sharpness of the solid block edges in the top row of the micromodel, the image for the experiment right after the plasma treatment indicates that half the solid blocks in the top row (the three blocks on the left in the top row in **Fig. 7b**) are surrounded by corner films. The evaporation rate can thus be approximated by **Equation 2**:

$$J_{right-after} = la\frac{M_v}{RT}\frac{D_v}{\delta}(p_{vs} - p_{v\infty}) \tag{2}$$

In this equation, M_v is the water molecular weight, R is the ideal gas constant, T is the temperature, p_{vs} is the saturated vapor pressure, $p_{v\infty}$ is the vapor partial pressure in the surrounding air, a is the thickness of the micromodel layer containing the channels (a = 1 mm), l is the active evaporation length along the micromodel top edge (thus $l \approx 0.5W$ where W is the micromodel width [W = 1.8 cm, **Fig. 1**]), and based on the region where corner films are present along the micromodel top edge in **Figure 7b**, δ is the external transfer characteristic length ($\delta \approx a$ from the results reported in [4]).

Based on the image in **Figure 7a** for the experiment performed one month after the plasma treatment, let us assume that the evaporation front is within the micromodel (no film around the majority of the solid blocks in the red dashed box in **Fig. 7a**). The evaporation rate is therefore expressed for this

experiment as **Equation 3**, where h is the position of the evaporation front measured from the top edge of micromodel.

$$J_{one-month-after} = Wa\frac{M_v}{RT}D_v\left(\delta + \frac{h}{\varepsilon}\right)^{-1}(p_{vs} - p_{v\infty}) \tag{3}$$

This expression is obtained using **Equation 4**, where p_{vi} is the water vapor partial pressure the surface of the micromodel, to express the diffusive mass transfer rate within the micromodel (tortuosity effects are neglected for the square network considered) and by combining the vapor diffusive transport external resistance and the resistance within the micromodel. This then leads to **Equation 5**.

$$J_{one-month-after} = Wa\frac{M_v}{RT}\varepsilon D_v\frac{(p_{vs} - p_{vi})}{h} \tag{4}$$

$$\frac{J_{right-after}}{J_{one-month-after}} \approx 0.5\left(1 + \frac{h}{\varepsilon\delta}\right) \tag{5}$$

From the data plotted in **Figure 8**, this ratio is equal to 8.5 for $S = 0.4$, which leads to $h \approx 8\ \mathrm{mm}$, which corresponds to an equivalent flat evaporation front position in the region of the third row of solid blocks from the micromodel top in **Figure 7a**. This position is consistent with the pattern shown in **Figure 7a,** suggesting that the zone in the dashed red box is dry in **Figure 7a,** whereas the significantly greater evaporation rate for the experiment right after the plasma treatment is consistent with the visible presence of corner films in the red dashed box in **Figure 7b**.

The variation of the drying kinetics in **Figure 8** for the experiment performed right after the plasma treatment is also consistent with the patterns depicted in **Figure 6** and the impact of corner films. For instance, there are less channels filled with liquid in the top row of the micromodel between the patterns for $S = 0.9$ (5 fully filled channels out of 7 channels) and $S = 0.7$ (3 fully filled channels). This is consistent with the decrease in the evaporation rate in **Figure 8** between these two values of saturation, as the evaporation rate from a channel is lower in the presence of corner films with the bulk invaded by the gas phase compared to a channel fully filled with liquid (4). The decrease in the evaporation rate after the relatively short plateau visible in **Figure 8** (overlap with the black dashed line) is also consistent with the pattern evolution, as the changes in the solid block edge sharpness in **Figure 6** suggest that the corner films gradually disappear in the top row as the saturation varies from 0.5 to 0.3.

3.5. Final deposit

The final particle deposit in the micromodel for both experiments with particles is depicted in **Figure 9**. As can be seen from **Figure 7b**, the final deposit is quite different between both experiments. The final particle deposit is much less spread over the network in the case of the experiment performed right after the plasma treatment with two main horizontal lines of deposit. The deposit is localized in the top region (entrance region) of the micromodel, primarily along the entire top edge of micromodel and in the next row of horizontal channels.

It is well known that colloidal particles are transported by diffusion and convection in the liquid phase during drying (11, 34). Diffusion tends to uniformize the particle concentration over the porous medium, whereas the convective flow induced in the liquid by the evaporation process tends to cause the accumulation of particles toward the evaporative regions (the open edge of micromodel at the beginning of the experiments). The competition between both transport phenomena is classically characterized by the Péclet number (19), which is defined and computed in **Appendix D** (available online). The greater the Péclet number above 1, the greater is the convective transport dominant compared to diffusion. The Péclet number estimate in **Appendix D** leads to a Péclet number value of the order of 104 for the experiment performed one month after the plasma treatment, which is thus still greater (by about a factor 6) in the case of the experiment performed right after the plasma treatment. Based on the sole consideration of this high value, one would expect that the particles accumulate at

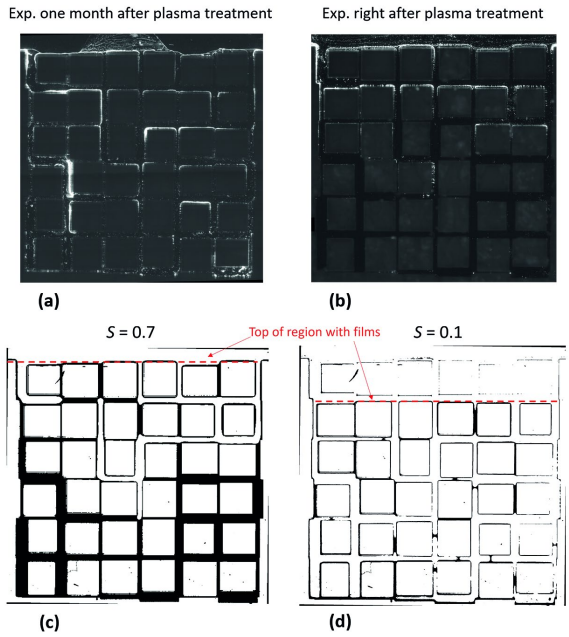

Figure 9: Final particle deposit (in bright light whitish/grey) in the micromodel for the experiment conducted one month after the plasma treatment **(a)** and directly following the plasma treatment **(b)**. Images of the liquid distribution for **(c)** $\boldsymbol{S = 0.7}$ and **(d)** $\boldsymbol{S = 0.1}$ in the case of the experiment conducted directly after the plasma treatment. The red dashed lines approximately indicate the position of the evaporation front (top of corner film region) based on the sharpness of the solid blocks. The places where the particles accumulate correspond to the brighter and clearer zones in the images.

the top surface of the micromodel (19). This is consistent with the fact that a deposit is visible along the entire top edge of the micromodel, i.e. at the entrance of the micromodel. However, the situation is in fact subtler. Since the convective effect is strongly dominant, it is expected that the particles are transported toward regions of the liquid–gas interface where evaporation takes place. For this reason, the particle convective transport is also expected to occur in the corner films since evaporation occurs at the tip of the corner films (4, 36). Accumulation of the particles in the corner films is thus expected as observed in a single channel (17). In other words, preferential particle accumulation is expected at the tip of the film region when films can develop over a significant region of the micromodel.

The two main lines of particle deposit in **Figure 9b** are consistent with a significant effect of the corner films and the patterns shown in **Figure 8**. As also illustrated in **Figure 9 c** & **d**, the top of the region with corner films stays at the top of the micromodel over a significant duration in the case of the experiment performed right after the plasma treatment (as shown in **Figure 9c**, this is the case for S as low as 0.7). Similarly, as illustrated by the red line in **Figure 9d**, the top of the region with corner films stays along the top of the second row of solid blocks in the micromodel over a significant period (up to at least $S = 0.1$, as illustrated in **Figure 9d**).

As a result of particle accumulation in the upper region, there are noticeably fewer particles present in the lower region over time. This should explain why there is a scarcity of particle deposition in the lower region of the micromodel.

The deposit pattern obtained in **Figure 9b** is consistent with the consideration that the corner liquid film subnetwork remains connected and attached to the micromodel entrance region for an extended period of time in the case of the experiment conducted immediately after the plasma treatment.

The deposit is noticeably less localized in the upper region of the micromodel for the experiment performed one month after the plasma treatment as particle deposits are visible in both the upper and the lower region of the micromodel in **Figure 9a**. However, the deposit is quite heterogeneous, with some channels having a clear and noticeable deposit whereas in other channels the particle deposit seems quite weak. It can be noted that the deposit in a channel is often seen along one side of the channel (**Fig. 10b**).

It is known that the considered micromodel structure favors the formation of "capillary rings" (48), which refer to liquid trapped in the corners around the solid cube-like blocks in the micromodel (**Fig. 10a**). Similar secondary capillary structures are expected in our micromodel. The consideration is that the particle deposits visible in **Figure 9a** form when these pieces of corner films eventually dry out.

The comparison between the drying pattern in **Figure 7a** and the deposit pattern in **Figure 9a** indicates that the channel corner deposit occurs preferentially in channels invaded early, i.e. larger channels, rather than in the narrower channels, which on average are invaded later by the gas phase. Consistent with the discussion of the drying kinetics in Section 3.4, the deposit pattern in **Figure 6a** suggests that the corner films do not form a well-connected subnetwork in the case of the experiment performed one month after the plasma treatment. Some isolated corner films form in some channels. Deposit in a channel corner would form when liquid trapped in the considered corners eventually evaporates. Due to the wettability difference between the SUEX and PDMS cover plate, it is expected that the deposit is in the SUEX corners (channel lower corners), as indicated by an experiment with a single channel (17). Due to the convective effect, which is the transport of the particles toward the evaporative menisci and the particle accumulation in the corner films, the concentration in particles is expected to decrease in the narrower channels, which on average are invaded at a later time point than the bigger channels. This would explain why the particle deposit is markedly less in the corners of the channels which are invaded later in the drying process.

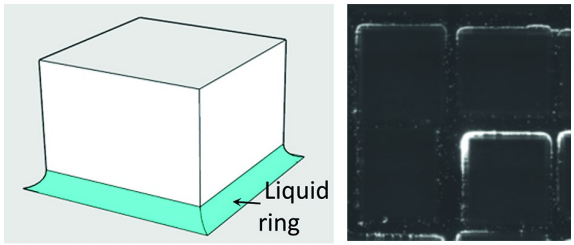

(a) **(b)**

Figure 10: (a) Schematic (artist view not based on the computation of the liquid gas–interface) of the liquid ring in the corners at the bottom of the solid block in the micromodel. **(b)** Illustration of the "corner deposit".

In summary, the difference in the corner film subnetwork connectivity would explain the striking difference between both particle deposit patterns, as shown in **Figure 9,** consistently with the difference in the wetting properties between both experiments. The lower contact angles in the experiment performed right after the plasma treatment favor thicker films, and possibly the formation of corner films in the channel's four corners (**Fig. 5**), which would lead to a well-connected corner film subnetwork (as sketched in **Fig. 11**). By contrast, the greater contact angles in the experiment performed one month after the plasma treatment lead to thinner films forming only in the SUEX corners (**Fig. 5**), and resulting in a poorly connected corner film subnetwork (as sketched in **Fig. 11**). This is also consistent with the significantly faster drying in the experiment performed right after the plasma treatment (**Fig. 3**). In other words, the comparison presented in this section illustrates the impact of liquid films on the distribution of particles during drying in the relatively low concentration limit under consideration.

As final remarks, it's worth noting that only three experiments were presented in this study. That being said, it should be emphasized that additional experiments were conducted, as detailed in reference (16), which confirmed the reproducibility and robustness of the results, particularly in the case of experiments performed one month or more after the plasma treatment. However, the experiment performed directly after the plasma treatment was not repeated. Although it would be desirable to repeat the experiment, it can be noted that the results on the particle localization in the micromodel in relation with the impact of corner films are fully consistent with the film visualization in the micromodel (sharpness of solid block edges), and with the observed faster drying, i.e. with a better-connected corner film subnetwork with thicker films.

4. CONCLUSIONS

Drying experiments with a micromodel in the presence of particles were reported. The comparison with a pure water experiment shows that the drying patterns are weakly impacted by the presence of the particles in the considered experiments. This also holds for the drying kinetics. The consideration of the Péclet number is not sufficient to infer the localization of the deposit in the micromodel. The Péclet number is quite high (O[10^4] at least) in the presented experiments. Nevertheless, the particles can be present in channels located away from the very top of the network at the end of drying.

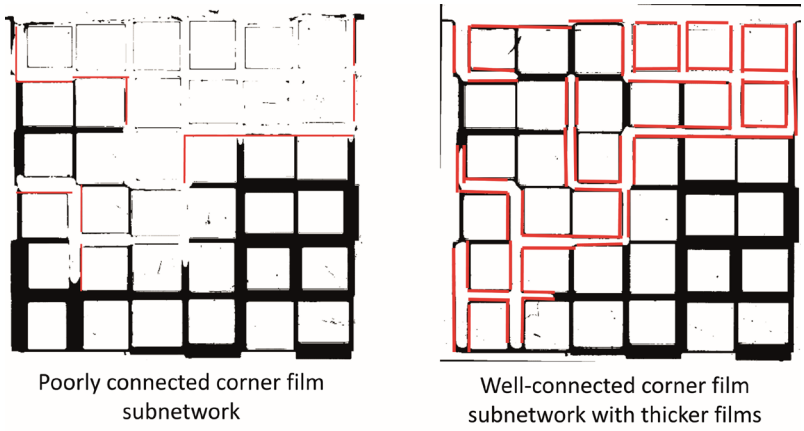

Figure 11: Sketch of a poorly connected corner film subnetwork (in red) with thinner films for the less wetting conditions, and of a well-connected corner film subnetwork (in red) with thicker films for the most wetting conditions.

As shown by the experiments after fresh or aged plasma treatment (that is with different wettability properties), secondary capillary structures (corner liquid wedges in our case) can have a strong impact on the final deposit distribution due to the particle transport in these secondary capillary structures. Even when the corner liquid film subnetwork is not well hydraulically connected, the corner liquid films are a preferred location for deposit, at least for the low particle concentration which was considered. In this respect, it would be interesting to study the evolution of these corner films during drying in relation to the particle transport in the films. This could help understand why corner deposit is noticeable in some channels and negligible in others.

Only a low concentration in particles was considered. It would be interesting to vary the concentration so as to study its impact on the results.

As a final remark, one has to keep in mind that drying in a quasi-2D network of interconnected channels is different from drying in a 3D porous medium due to different percolation properties of the liquid phase. The period over which the liquid phase fully fills pores and forms a percolating phase, without considering the possible hydraulic connectivity associated with the corner films, lasts much longer in 3D than in 2D (36). This should favor the greater accumulation of particles in the top region of the medium. However, the fact corner films can be a pathway for particle transport, as illustrated in the present article, is generic, i.e. a common feature in 2D and in 3D.

STATEMENTS AND DECLARATIONS

Supplementary Material

See **Appendix A** for information on "Imaging the Final Deposit", **Appendix B** for information on the"Corner Film Model", and **Appendix C** for information on "Patterns – Comparison with Pure Water Experiment", and **Appendix D** with information on the "Péclet Number Evaluation", which can be found online with this paper here.

Acknowledgements

The authors are grateful to Julien Lefort (IMFT) and Sebastien Cazin (IMFT) for the help provided during the experiments.

Author Contributions

Elisa Ghiringhelli: Investigation, Formal analysis, Writing – review & editing. **Manuel Marcoux:** Methodology, Supervision, Writing – review & editing. **Sandrine Geoffroy:** Software. **Marc Prat:** Conceptualization, Formal analysis, Writing – original draft - Writing – review & editing.

Conflicts of Interest

The authors report that there are no conflicts of interest to declare.

Data, Code & Protocol Availability

Data will be made available upon reasonable request.

ORCID IDs

Elisa Ghiringhelli https://orcid.org/0009-0009-3911-6370
Manuel Marcoux https://orcid.org/0000-0001-5052-3588
Sandrine Geoffroy https://orcid.org/0000-0002-8376-9143
Marc Prat https://orcid.org/0000-0001-8685-6595

REFERENCES

1. Bodas, D. & Khan-Malek, C (2006). Formation of more stable hydrophilic surfaces of PDMS by plasma and chemical treatments. *Microelectronic Engineering,* 83, 1277–1279. https://doi.org/10.1016/j.mee.2006.01.195
2. Brakke, K. A. (1992). The surface evolver. *Experimental Mathematics*, 1(2), 141–165. https://doi.org/10.1080/10586458.1992.10504253
3. Chapuis, O., & Prat, M. (2007). Influence of wettability conditions on slow evaporation in two-dimensional porous media. *Physical Review E*, 75(4), 046311. https://doi.org/10.1103/PhysRevE.75.046311.
4. Chauvet, F., Duru, P., Geoffroy, S., & Prat, M. (2009). Three periods of drying of a single square capillary tube. *Physical Review Letters*, 103(12), 124502. https://doi.org/10.1103/PhysRevLett.103.124502
5. Chen, C., Duru, P., Joseph, P., Geoffroy, S., & Prat, M. (2017). Control of evaporation by geometry in capillary structures. From confined pillar arrays in a gap radial gradient to phyllotaxy-inspired geometry. *Scientific Reports*, 7(1), 15110. https://doi.org/10.1038/s41598-017-14529-z
6. Chen, C., Joseph, P., Geoffroy, S., Prat, M., & Duru, P. (2018). Evaporation with the formation of chains of liquid bridges. *Journal of Fluid Mechanics*, 837, 703–728. https://doi.org/10.1017/jfm.2017.827
7. Chraïbi, H., Prat, M., & Chapuis, O. (2009). Influence of contact angle on slow evaporation in two-dimensional porous media. *Physical Review E*, 79(2), 026313. https://doi.org/10.1103/PhysRevE.79.026313
8. DeCarlo, K. F., & Shokri, N. (2014). Effects of substrate on cracking patterns and dynamics in desiccating clay layers. *Water Resources Research*, 50(4), 3039–3051. https://doi.org/10.1002/2013WR014466
9. Freitas, D.S., Prat, M (2000). Pore Network Simulation of Evaporation of a Binary Liquid from a Capillary Porous Medium. *Transport in Porous Media*, 40, 1–25. https://doi.org/10.1023/A:1006651524722
10. Diouf, B., Geoffroy, S., Chakra, A. A., & Prat, M. (2018). Locus of first crystals on the evaporative surface of a vertically textured porous medium. *The European Physical Journal Applied Physics*, 81(1), 11102. https://doi.org/10.1051/epjap/2018170340
11. Dufresne, E. R., Corwin, E. I., Greenblatt, N. A., Ashmore, J., Wang, D. Y., Dinsmore, A. D., Cheng, J. X., Xie, X. S., Hutchinson, J. W., & Weitz, D. A. (2003). Flow and fracture in drying nanoparticle suspensions. *Physical Review Letters*, 91(22), 224501. https://doi.org/10.1103/PhysRevLett.91.224501
12. Eloukabi, H., Sghaier, N., Ben Nasrallah, S., & Prat, M. (2013). Experimental study of the effect of sodium chloride on drying of porous media: The crusty–patchy efflorescence transition. *International Journal of Heat and Mass Transfer*, 56(1–2), 80–93. https://doi.org/10.1016/j.ijheatmasstransfer.2012.09.045
13. Faiyas, A. P. A., Erich, S. J. F., Huinink, H. P., & Adan, O. C. G. (2017). Transport of a water-soluble polymer during drying of a model porous media. *Drying Technology*, 35(15), 1874–1886. https://doi.org/10.1080/07373937.2017.1283515
14. Fantinel, P., Borgman, O., Holtzman, R., & Goehring, L. (2017). Drying in a microfluidic chip: Experiments and simulations. *Scientific Reports*, 7(1), 15572. https://doi.org/10.1038/s41598-017-15718-6
15. Geistlinger, H., Ding, Y., Apelt, B., Schlüter, S., Küchler, M., Reuter, D., et al (2019). Evaporation Study Based on Micromodel Experiments: Comparison of Theory and Experiment. *Water Resources Research*, 55(8), 6653-6672. https://doi.org/10.1029/2018WR024647

16. Ghiringhelli, E (2023). Evaporation in model porous media with transport of particles. Fluids mechanics [physics.class-ph]. Université Paul Sabatier - Toulouse III, 2023. English. ⟨NNT : 2023TOU30147⟩. ⟨tel-04329675⟩. https://theses.hal.science/tel-04329675
17. Ghiringhelli, E., Marcoux, M., Geoffroy, S., & Prat, M. (2023). Evaporation in a single channel in the presence of particles. *Colloids and Surfaces A: Physicochemical and Engineering Aspects*, 656, 130432. https://doi.org/10.1016/j.colsurfa.2022.130432
18. Goehring, L., Nakahara, A., Dutta, T., Kitsunezaki, S., & Tarafdar, S. (2015). *Desiccation cracks and their patterns: Formation and modelling in science and nature.* Wiley-VCH, Verlag GmbH & Co. KGaA.
19. Huinink, H. P., Pel, L., & Michels, M. A. J. (2002). How ions distribute in a drying porous medium: A simple model. *Physics of Fluids*, 14(4), 1389–1395. https://doi.org/10.1063/1.1451081
20. Ito, H., Abe, K., Ishida, M., Nakano, A., Maeda, T., et al. (2014). Effect of through-plane distribution of polytetrafluoroethylene in carbon paper on in-plane gas permeability. *Journal of Power Sources*, 248, 822–830. https://doi.org/10.1016/j.jpowsour.2013.10.009
21. Keey, R. B., & Suzuki, M. (1974). On the characteristic drying curve. *International Journal of Heat and Mass Transfer*, 17(12), 1455–1464. https://doi.org/10.1016/0017-9310(74)90055-6
22. Keita, E., Faure, P., Rodts, S., & Coussot, P. (2013). MRI evidence for a receding-front effect in drying porous media. *Physical Review E*, 87(6), 062303. https://doi.org/10.1103/PhysRevE.87.062303
23. Keita, E. (2021). Particle deposition in drying porous media. *Materials*, 14(18), 5120. https://doi.org/10.3390/ma14185120
24. Kharaghani, A., Mahmood, H. T., Wang, Y., & Tsotsas, E. (2021). Three-dimensional visualization and modeling of capillary liquid rings observed during drying of dense particle packings. *International Journal of Heat and Mass Transfer*, 177, 121505. https://doi.org/10.1016/j.ijheatmasstransfer.2021.121505
25. Laurindo, J. B., & Prat, M. (1998). Numerical and experimental network study of evaporation in capillary porous media. Drying rates. *Chemical Engineering Science*, 53(12), 2257–2269. https://doi.org/10.1016/S0009-2509(97)00348-5
26. Laurindo, J. B., & Prat, M. (1998). Numerical and experimental network study of evaporation in capillary porous media. Drying rates. *Chemical Engineering Science*, 53(12), 2257–2269. https://doi.org/10.1016/S0009-2509(97)00348-5
27. Lazhar, R., Najjari, M., & Prat, M. (2020). Combined wicking and evaporation of NaCl solution with efflorescence formation: The efflorescence exclusion zone. *Physics of Fluids*, 32(6), 067106. https://doi.org/10.1063/5.0007548
28. Lewis, W. K. (1921). The rate of drying of solid materials. *Journal of Industrial & Engineering Chemistry*, 13(5), 427–432. https://doi.org/10.1021/ie50137a021
29. Liefferink, R. W., Naillon, A., Bonn, D., Prat, M., & Shahidzadeh, N. (2018). Single layer porous media with entrapped minerals for microscale studies of multiphase flow. *Lab on a Chip*, 18(7), 1094–1104. https://doi.org/10.1039/C7LC01377A
30. Lenormand, R., Touboul, E., & Zarcone, C. (1988). Numerical models and experiments on immiscible displacements in porous media. *Journal of Fluid Mechanics*, 189, 165–187. https://doi.org/10.1017/S0022112088000953
31. Merlin, A., Salmon, J.-B., & Leng, J. (2012). Microfluidic-assisted growth of colloidal crystals. *Soft Matter*, 8(13), 3526. https://doi.org/10.1039/c2sm07149e
32. Nachshon, U., Weisbrod, N., Dragila, M. I., & Grader, A. (2011). Combined evaporation and salt precipitation in homogeneous and heterogeneous porous media. *Water Resources Research*, 47(3), 2010WR009677. https://doi.org/10.1029/2010WR009677
33. Pillai, K. M., Prat, M., & Marcoux, M. (2009). A study on slow evaporation of liquids in a dual-porosity porous medium using square network model. *International Journal of Heat and Mass Transfer*, 52(7–8), 1643–1656. https://doi.org/10.1016/j.ijheatmasstransfer.2008.10.007
34. Pingulkar, H., & Salmon, J.-B. (2023). Confined directional drying of a colloidal dispersion: Kinetic modeling. *Soft Matter*, 19(12), 2176–2185. https://doi.org/10.1039/D3SM00058C
35. Prat, M. (2002). Recent advances in pore-scale models for drying of porous media. *Chemical Engineering Journal*, 86(1–2), 153–164. https://doi.org/10.1016/S1385-8947(01)00283-2
36. Prat, M. (2007). On the influence of pore shape, contact angle and film flows on drying of capillary porous media. *International Journal of Heat and Mass Transfer*, 50(7–8), 1455–1468. https://doi.org/10.1016/j.ijheatmasstransfer.2006.09.001
37. Pu, Y., Wang, W., Dorshow, R. B., & Alfano, R. R. (2012). *Picosecond polarization spectroscopy of fluorescein attached to different molecular volume polymer influenced by rotational motion* (C. Tabor, F. Kajzar, T. Kaino, & Y. Koike, Eds.; p. 825818). https://doi.org/10.1117/12.904692

38. Qazi, M. J., Bonn, D., & Shahidzadeh, N. (2019). Drying of salt solutions from porous media: Effect of surfactants. *Transport in Porous Media*, 128(3), 881–894. https://doi.org/10.1007/s11242-018-1164-5
39. Qin, F., Mazloomi Moqaddam, A., Kang, Q., Derome, D., & Carmeliet, J. (2019). LBM simulation of self-assembly of clogging structures by evaporation of colloidal suspension in 2D porous media. *Transport in Porous Media*, 128(3), 929–943. https://doi.org/10.1007/s11242-018-1157-4
40. Qin, F., Fei, L., Zhao, J., Kang, Q., Derome, D., & Carmeliet, J. (2023). Lattice Boltzmann modelling of colloidal suspensions drying in porous media accounting for local nanoparticle effects. *Journal of Fluid Mechanics*, 963, A26. https://doi.org/10.1017/jfm.2023.344
41. Rad, M. N., Shokri, N., Keshmiri, A., & Withers, P. J. (2015). Effects of grain and pore size on salt precipitation during evaporation from porous media. *Transport in Porous Media*, 110(2), 281–294. https://doi.org/10.1007/s11242-015-0515-8
42. Rieder, D. R., Peters, E. A. J. F., & Kuipers, J. A. M. (2023). Modeling the drying process of porous catalysts: Impact of the pore size distribution. *Industrial & Engineering Chemistry Research*, 62(46), 20006–20016. https://doi.org/10.1021/acs.iecr.3c03057
43. Rufai, A., & Crawshaw, J. (2017). Micromodel observations of evaporative drying and salt deposition in porous media. *Physics of Fluids*, 29(12), 126603. https://doi.org/10.1063/1.5004246 Ä
44. Scheel, M., Seemann, R., Brinkmann, M., Di Michiel, M., Sheppard, A., Breidenbach, B., & Herminghaus, S. (2008). Morphological clues to wet granular pile stability. *Nature Materials*, 7(3), 189–193. https://doi.org/10.1038/nmat2117
45. Sghaier, N., Geoffroy, S., Prat, M., Eloukabi, H., & Ben Nasrallah, S. (2014). Evaporation-driven growth of large crystallized salt structures in a porous medium. *Physical Review E*, 90(4), 042402. https://doi.org/10.1103/PhysRevE.90.042402
46. Sherwood, T.K (1929). The Drying of Solids - I. *Industrial and Engineering Chemistry*. 21, 12-16. https://doi.org/10.1021/ie50229a004
47. Veran-Tissoires, S., & Prat, M. (2014). Evaporation of a sodium chloride solution from a saturated porous medium with efflorescence formation. *Journal of Fluid Mechanics*, 749, 701–749. https://doi.org/10.1017/jfm.2014.247
48. Vorhauer, N., Wang, Y. J., Kharaghani, A., Tsotsas, E., & Prat, M. (2015). Drying with formation of capillary rings in a model porous medium. *Transport in Porous Media*, 110(2), 197–223. https://doi.org/10.1007/s11242-015-0538-1
49. Vorhauer, N., Tsotsas, E., & Prat, M. (2018). Temperature gradient induced double stabilization of the evaporation front within a drying porous medium. *Physical Review Fluids*, 3(11), 114201. https://doi.org/10.1103/PhysRevFluids.3.114201
50. Wilkinson, D., & Willemsen, J. F. (1983). Invasion percolation: A new form of percolation theory. *Journal of Physics A: Mathematical and General*, 16(14), 3365–3376. https://doi.org/10.1088/0305-4470/16/14/028
51. Wu, R., Zhang, T., Ye, C., Zhao, C. Y., Tsotsas, E., & Kharaghani, A. (2020). Pore network model of evaporation in porous media with continuous and discontinuous corner films. *Physical Review Fluids*, 5(1), 014307. https://doi.org/10.1103/PhysRevFluids.5.014307
52. Wu, R. & Prat, M. (Eds). (2022). *Mass Transfer Driven Evaporation from Capillary Porous Media*. Taylor & Francis. https://doi.org/10.1201/9781003011811
53. Wu, R. & Chen, F. (2023). Interplay between salt precipitation, corner liquid film flow, and gas–liquid displacement during evaporation in microfluidic pore networks. *Journal of Applied Physics*, 133, 074701. https://doi.org/10.1063/5.0135135
54. Yiotis, A. G., Boudouvis, A. G., Stubos, A. K., Tsimpanogiannis, I. N., & Yortsos, Y. C. (2004). Effect of liquid films on the drying of porous media. *AIChE Journal*, 50(11), 2721–2737. https://doi.org/10.1002/aic.10265
55. Yiotis, A. G., Salin, D., Tajer, E. S., & Yortsos, Y. C. (2012). Drying in porous media with gravity-stabilized fronts: Experimental results. *Physical Review E*, 86(2), 026310. https://doi.org/10.1103/PhysRevE.86.026310